Letter

Relating Electronic and Geometric Structure of Atomic Layer Deposited BaTiO₃ to its Electrical Properties
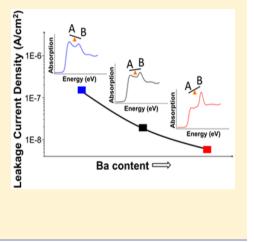
Jan Torgersen,*,⊥,† Shinjita Acharya,⊥,† Anup Lal Dadlani,⊥,‡ Ioannis Petousis,§ Yongmin Kim,† Orlando Trejo,† Dennis Nordlund,∥ and Fritz B. Prinz†,§

†Department of Mechanical Engineering, ‡Department of Chemistry, and §Department of Materials Science and Engineering, Stanford University, Stanford, California 94305, United States

∥Stanford Synchrotron Radiation Lightsource, SLAC National Accelerator Laboratory, Menlo Park, California 94025, United States

Ⓢ *Supporting Information*

ABSTRACT: Atomic layer deposition allows the fabrication of BaTiO₃ (BTO) ultrathin films with tunable dielectric properties, which is a promising material for electronic and optical technology. Industrial applicability necessitates a better understanding of their atomic structure and corresponding properties. Through the use of element-specific X-ray absorption near edge structure (XANES) analysis, O K-edge of BTO as a function of cation composition and underlying substrate (RuO₂ and SiO₂) is revealed. By employing density functional theory and multiple scattering simulations, we analyze the distortions in BTO's bonding environment captured by the XANES spectra. The spectral weight shifts to lower energy with increasing Ti content and provides an atomic scale (microscopic) explanation for the increase in leakage current density. Differences in film morphologies in the first few layers near substrate−film interfaces reveal BTO's homogeneous growth on RuO₂ and its distorted growth on SiO₂. This work links structural changes to BTO thin-film properties and provides insight necessary for optimizing future BTO and other ternary metal oxide-based thin-film devices.

The perovskite BaTiO₃ (BTO) exhibits high dielectric constants,[1,2] ferroelectricity,[3] piezoelectricity,[4] and photorefractive effects,[5] making it a promising material for electronic and optical devices. Using atomic layer deposition (ALD), BTO can be deposited as a ternary compound employing sequential BaO and TiO₂ cycles,[6−8] allowing for atomic level control of thickness, composition, and crystallinity.[9] Together with ALD's unique self-limiting surface reactions,[10] researchers foresee its potential in dynamic random-access memory applications,[11,12] in which BTO, conformally coated on high-aspect ratio trenches, may decisively contribute to increasing the memory density necessary for further device miniaturization. However, approaching the nanometer regime, key questions regarding the electronic structure determining the films' properties remain.

As for MgO/ZnO and Al₂O₃/ZnO ALD,[13,14] metal-oxide (MO) ALD typically renders multicomponent nanolaminate stacks with different materials spatially localized in discrete layers separated by sharp boundaries.[15] This characteristic is beneficial for BTO's substrate interface. However, its deposition as a ternary MO-ALD (AₓBᵧOᵤ) film gives rise to a conflicting condition; the fabrication now requires mixing binary A−O and B−O layer deposition cycles in a way to obtain the desired stoichiometry.[6,7,12,16] Postprocess annealing facilitates the formation of intermixed crystalline structures;[12,17] however, depending on the substrate, this may result in diffusion and subsequent interfacial layer mixing, eventually compromising film quality.[18] It is not clear how the local bonding environment

changes when employing a ternary MO deposition technique, to what extent BaO and TiO₂ mix, and how the substrate induces strain in the film.

BTO thin films' morphological and electronic properties, such as crystallinity, refractive index, dielectric constant, and leakage currents, are different from the bulk and hard to predict.[19−21] Tuning the composition of ALD BTO, researchers examined the rise of leakage current with Ti content and a dielectric constant maximum at stoichiometry.[7] Postprocess annealing partly crystallizes and densifies the as-deposited amorphous film, increasing its capacitance.[8,17] However, a chemical and structural explanation of these application-relevant findings is missing.

X-ray absorption near edge structure (XANES) is an emerging, powerful and promising characterization technique for compositional effects[22] and interfaces[23] in ultrathin ALD films. Its elemental specificity allows the probing of amorphous and crystalline films.[24,25] XANES provides oxidation states, coordination chemistry, molecular orbitals, and band structure, as well as local displacement and chemical short-range orders.[26] Analyzing the O K-edge of ALD BTO films, we investigate the mixing of the constituents TiO₂ and BaO and look into structural changes with composition, thickness, underlying
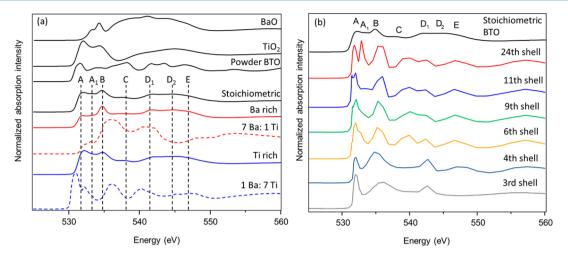
Figure 1. (a) O K-edge XANES spectra for ALD BaO, TiO$_2$, and BTO powder; stoichiometric ALD BTO, Ba-rich BTO, simulated Ba-rich BTO, Ti-rich BTO, and simulated Ti-rich BTO (top to bottom). Simulated spectra (dotted) are obtained using FEFF code[27,28] and were performed on a relaxed structure containing 7:1 (Ba-rich) and 1:7 (Ti-rich) Ba:Ti. Spectra were background subtracted and atomically normalized in the energy region from 539 to 548 eV. The reference ALD sample for the O K-edge depicts five main features. (b) Theoretical MS calculations as a function of the cluster size (number of shells: 3, 4, 6, 9, 11, and 24) for tetragonal BTO, where a shell refers to a group of atoms at a particular distance from the absorbing atom. The 24-shell cluster corresponds to a sphere with a radius of 10 Å. The experimental stoichiometric ALD BTO is shown at the top as a reference.
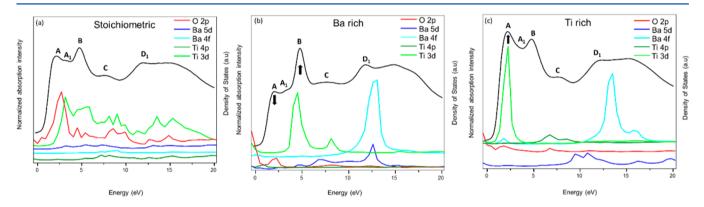

Figure 2. Simulated pDOS relative to the Fermi level in comparison to the respective experimental spectra. The total density of states is shifted such that the onset of the band gap is at 0 eV, and the spectra are aligned by matching the maximum intensity of the first peak to the maximum pDOS intensity of the absorbing atom. (a) Stoichiometric BTO showing mainly O 2p and Ti 3d hybridization with minimal orbital contributions from Ba 5d, Ba 4f, and Ti 4p to the conduction band; (b) Ba-rich BTO showing mainly O 2p−Ti 3d hybridized orbitals near the onset and O 2p−Ba 5d−Ba 4f hybridization 12.5 eV after the main edge; and (c) Ti-rich BTO showing the transition from O 1s to O 2p−Ti 3d at the onset, and O 1s to O 2p− Ba 4f 14 eV above the Fermi level.

substrate, and postprocess annealing. In addition, density functional theory (DFT) and multiple scattering (MS) simulations allow the derivation of structural estimates, which allow insight into the structural changes leading to the obtained leakage current densities.

In Figure 1, we first look at the top four O K-edge spectra of ALD BaO, TiO$_2$, cubic powder BTO and nearly stoichiometric ALD BTO (Ba:Ti ∼ 0.9; 10 nm; details about sample preparation are in the Supporting Information) deposited on RuO$_2$. Without any further treatment, all of these ALD BTO samples are amorphous after deposition.[6,8,17] Hence, the comparison provides insight into the mixing during BTO's thin-film deposition. We use the cubic BTO powder as a reference to assign peaks.[29−31] Peaks A−E correspond to the electronic excitation from O 1s states to several unoccupied states in the conduction band. Peak A indicates a transition from O 1s to O 2p−Ti 3d hybridized states, linking it to the t$_{2g}$ crystal field peak. This is corroborated by the partial density of states (pDOS) calculation (Figure 2a; details of the crystal

structure used for pDOS and calculation details are shown in the Supporting Information, Table S3 and Figure S6). The conduction band is mostly composed of these states with minor contributions from Ba 5d, Ba 4f, and Ti 4p orbitals. Peak A$_1$ stems from the same transition and is visible in our amorphous samples. It represents asymmetric Ti−O−Ti bonding environments.[29] This is contrary to the cubic BTO powder reference and hints toward a distortion. Feature B resembles the e$_g$ crystal field peak, and peak C results from a transition from O 1s to O 2p−Ba 5d hybridized states along with strong MS contributions (Figure S7). Peaks D$_1$ and D$_2$ derive from an O 1s transition to O 2p−Ba 4f states with MS contributions (Figure S7).

BTO thin films with thickness below 50 nm cannot become cubic even when grown on substrates with similar perovskite lattices because of biaxial substrate constraints.[32] Using FEFF code, we therefore approached the stoichiometric ALD BTO structure simulating O K-edge spectra for a tetragonal BTO as a function of the cluster size (atomic shells of 3, 4, 6, 9, 11 and 24; Figure 1b, Table S3, and Figure S6a show details on the
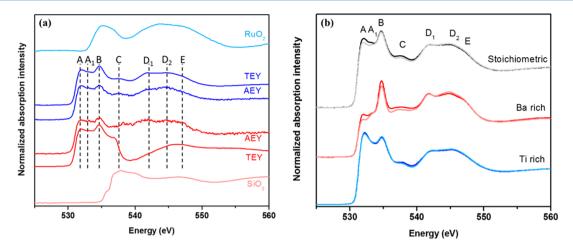
Figure 3. (a) TEY and AEY O K-edges XANES spectra of 10 nm stoichiometric BTO grown on RuO_2 (blue) and SiO_2 (red), plotted with the O K-edge of bare RuO_2 (light blue) and SiO_2 (light red) as references. (b) O K-edge of stoichiometric, Ba-rich and Ti-rich samples before and after 3 h of O_2 plasma treatment (250 W, 15 mTorr). Light and dark colors indicate samples before and after plasma treatment, respectively.

tetragonal BTO input file). Feature E starts developing with the fourth shell (short-range order), while feature D_1 appears from the sixth shell (midrange order); both features are predominantly a result of MS. Interestingly, feature A splits into A and A_1 in shell 11, indicating the asymmetric position of the nearest Ti with respect to the excited O.[29] This distortion of the TiO_6 octahedron was theoretically predicted to evolve in perovskites with sufficient distortion from the cubic phase, distortions that include strain or defects in thin films.[30] It appears in our experimental stoichiometric and Ba-rich samples. Despite this distortion, the ALD BTO bears resemblance to tetragonal BTO. It cannot be derived from a linear combination of TiO_2 and BaO (Figure S1a), indicating its intermixed nature. Ba M5, M4 edge XANES spectra (Figure S4) further strengthen this argument. This confirms earlier indications from X-ray photoelectron spectroscopy[6] (Figure S1c).

Tailoring ALD BTO's dielectric performance to device-specific needs simply requires altering the BaO:TiO_2 cycle ratio within the deposition.[7] To understand the electronic structure changes with composition, we deposited stoichiometric (Ba:Ti $\sim$ 0.9, black), Ba-rich ($\sim$1.4, solid red), and Ti-rich ($\sim$0.6, solid blue) films. Their O K-edge spectra can be seen in Figure 1a. The dotted lines underneath the experimental BTO spectra illustrate simulated O K-edge spectra obtained on relaxed BTO clusters derived from DFT. Containing 7:1 (red) and 1:7 Ba:Ti (blue), the two BTO crystals of compositional extremes (details in Table S3 and Figure S6) best match the experimental spectra. The simulations capture salient features in the near-edge X-ray absorption fine structure (NEXAFS) region; however, they do not depict features at higher energy. A better match would require simulating all possible local environments, which is not essential for the properties investigated in this study.

The Ba-rich (red) sample has a weaker edge jump than the stoichiometric one, a split of A into A and A_1, a very intense peak B, a low-intensity feature C, and a peak D_1 that is most resolved compared to all other samples. Features D_2 and E remain unchanged. Here, we observe a more discrete mixing of the pDOS. Distortion of the structure lowers the hybridization, as can be seen in films off-stoichiometry. The Ti 3d orbital contribution shifts to higher energies (Figure 2b). In contrast to the stoichiometric case, the conduction band comprises Ti 4p and high-energy Ba 4f and 5d states hybridized with O 2p

also.[31] The increase of B (marked by arrow) and a splitting of A derives from Ti−O−Ti asymmetric bond distances in the BTO lattice, leading to a more pronounced electron density depletion on one side of Ti than on the other.[29] This lattice distortion seems larger with more Ba content, which is also observable in the pre-edge of Ti L3 spectra (Figure S3a). The onset of the simulated Ba-rich spectra occurs at higher energy than the experimental Ba-rich case. Though this shift is not as apparent in the experimental Ba-rich sample, it provides a qualitative explanation of the higher band gap (Table S2) and lower leakage current density (Figure 4).

In contrast, the intensity ratio of A to B becomes larger (marked by arrow) in the Ti-rich sample (blue). Feature A_1 is not present, either because the strong feature A masks A_1 or no splitting occurs. Features C−E appear similar to the stoichiometric reference. The low-energy shift of the major Ti 3d orbital contribution to BTO's conduction band raises feature A (pDOS in Figure 2c). Similar to the Ba-rich case, we also observe Ba 4f and 5d contributions at higher energies. However, the onset of the simulated curve is now earlier and the spectral weight shifts to lower energies towards the beginning of the spectrum. The band gap decreases with the Ti content, which is in agreement with experimental findings on band gap (Table S2) and the obtained leakage current density (Figure 4).[7]

XANES and pDOS calculations therefore allow explaining compositional effects to BTO's band gap and their relation to the obtainable leakage current density.

In addition to the composition, the underlying substrate can largely affect thin-film BTO's properties; such properties are markedly different from those of the bulk material due to strain or diffusion at the substrate interface.[32,33] Here, we compare the O K-edge of 10 nm thick stoichiometric BTO films deposited onto SiO_2 and RuO_2 substrates (Figure 3a), the preferred substrates for thin-film BTO device fabrication.[6,7,17] Auger electron yield (AEY) and total electron yield (TEY) provide information on the film's surface and bulk, respectively. For comparison, the O K-edge of native RuO_2 and SiO_2 is shown above and below the respective BTO spectra.

The RuO_2 reference spectrum (light blue) is similar to that in the literature.[34,35] The first broad feature (534−536 eV) derives from the excitation of O 1s into O 2p and Ru 4d hybridized states, whereas the higher-energy feature (starting from 543
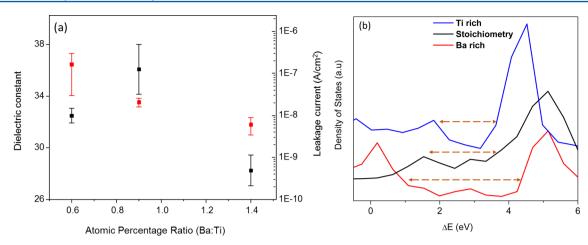
Figure 4. (a) Dielectric constant (black squares, 1 KHz frequency, 0 V applied bias) and corresponding leakage currents densities (red squares, + 1.6 V applied bias) of stoichiometric, Ba-rich, and Ti-rich BTO samples; MIM capacitor ($Pt/BTO/RuO_2/Ru$) with BTO thickness of 15 nm, plasma treated for 3 h. Note that leakage current densities under positive bias means electrons are injected from the bottom Ru substrate to BTO. Standard deviation is reported for 5 measurements in each case. (b) The total DOS with increasing Ba content (bandgap region).

eV) shows O 2p−Ru 5sp hybridized states. The TEY and the AEY of BTO grown on RuO_2 (blue) share the same features, which suggests that BTO's structure in the first few layers near the substrate interface is similar to the one on the surface. The SiO_2 reference spectrum (light red) has all the characteristic peaks described in the literature,[36] mainly consisting of an excitation of O 2p−Si 3p hybridized orbitals (535−540 eV). The AEY spectrum of BTO grown on RuO_2 (blue) and on SiO_2 (red) are similar, whereas the respective TEY spectra differ. The bonding environment deeper in the film is different in the higher-energy region of the spectrum (from 538 eV).

RuO_2 readily reacts with a wide range of metal precursors leading to the formation of interfacial mixed MO films ($Ba_xTi_yRu_zO_w$, intermediate of BTO and RuO_2)[12] with lattices similar to the BTO film. This minimizes interfacial strain.[37] On the other hand, formation of an interfacial layer is less likely on a stable SiO_2.[7] The lattice mismatch at the interface may cause the growth of a strained film, inducing distortions to the BTO structure, distortions that decrease with film thickness because of the relaxation of dislocations.

The "critical thickness" at which BTO is completely relaxed is inversely proportional to the lattice mismatch and depends on the substrate.[38] We compare 5, 10, and 15 nm thick stoichiometric samples deposited on RuO_2 and SiO_2. We do not observe a trend in the O K-edge (Figure S2) nor in the Ti L3 and L2 edges (Figure S3b) on either substrate. Hence, relaxation events in the reported thickness regime seem unlikely. Studies on larger thickness variations might reveal the substrate-specific "critical thicknesses." At the vacuum interface, the film may still adopt a relaxed structure when deposited on SiO_2 substrates, as inferred from its AEY spectra.

Postprocess annealing introduces crystallite grains of either cubic, tetragonal, or rhombohedral phases in the thin-film BTO, increasing its density.[17] This affects its dielectric constant and leakage current.[7] The O K-edge spectra of 3 h plasma treated and untreated as-deposited (AD) samples are shown in Figure 3b. The intensity increase of peak A in all the samples indicates a shift of the DOS towards lower energies. This hints at the evolution of Ti−O−Ti bond symmetry[29] facilitated after BTO's relaxation to a thermodynamically more stable arrangement. The changes in the peak intensity are most pronounced in the Ba-rich case, where, as per our previous assumption, the lattice

is most distorted compared to the other compositions. The Ti K-edge of ALD samples (Figure S5) displays a perovskite typical pre-edge (feature A),[39] larger and slightly shifted to lower energy than cubic BTO. This indicates a displacement of Ti^{4+} cations from the center of the TiO_6 octahedron. The feature does not seem to change with plasma treatment, whereas the main edge peaks (B and C) develop, pointing toward a change in Ti 4p hybridization.

The dielectric properties of thin-film BTO strongly depend on the Ba:Ti ratio and the morphology of the film.[8,12,17] Film thinness[40] and low crystallinity[32,41] limit the achievable dielectric constants. The dielectric constants (Figure 4a) are similar to those obtained on 12 nm thick ALD BTO MIS devices[7] and lower than those on 32 nm thick thermally annealed MIM devices.[8] The lower dielectric constant compared to the latter results from (1) the thinness and (2) limited crystallinity of our samples.

The leakage currents observed are lower than on ALD BTO-based MIS devices,[7] which is likely due to the slightly thicker films investigated in this work.[42] Interestingly, 32 nm thick thermally annealed MIM devices have higher leakage current densities.[8] In polycrystalline films, grain boundaries may act as preferred leakage paths leading to higher leakage current densities than in amorphous films.[43] This can be shown gradually crystallizing the film with postprocess O_2 plasma.[17] Both dielectric constant and leakage current densities increase with plasma duration (Figure S10). An optimization of BTO MIM devices involves a trade-off between dielectric constant and leakage current. A separate study is intended but beyond the scope of this work.

Regarding the trend in leakage current densities with film composition, we observe an inverse proportionality to the band gap, which determines the barrier height for electrons flowing from the top electrode (Figure 4b).[7] Two opposing composition-dependent mechanisms, (1) covalency and (2) ionicity, both related to the Ti−O and Ba−O average bond distances (Ti−O and Ba−O, Table S4), may constitute the underlying mechanism. In the Ba-rich case, the Ba−O bond length is longest, increasing the material's ionicity, which generally leads to a higher band gap.[44] Ba−O bond lengths are similar in the stoichiometric and Ti-rich case. The increase in band gap at stoichiometry with respect to the Ti-rich case stems

from the larger Ti−O bond lengths, a product of decreased covalency. In the Ti-rich case, a strong presence of Ti 3d states in the lower part of the conduction band is observed, (Figure 2c (light green)) causing the highest leakage current density in this sample.

In summary, we have elaborated on the local chemical and structural modifications of thin-film BTO depending on ALD process parameters like $BaO:TiO_2$ cycle ratio and plasma duration as well as the choice of the substrate. Analyzing the XANES O K-edge, we have shown that the sequential deposition of TiO_2 and BaO layers results in the formation of an intermixed ternary MO that can be associated with a distorted BTO. With increasing Ti content in the film, the pDOS reveals the shift of O 2p−Ti 3d hybridized states to lower energies. Furthermore, SiO_2 as the substrate constrains BTO growth, whereas the film is homogeneous throughout on RuO_2, which is likely a result of interfacial layer formation. Finally, postplasma annealing introduces Ti−O−Ti bond symmetry through relaxation events, which is most pronounced in Ba-rich films.

Linking structural changes to ALD process parameters, this work provides new insight on BTO as a thin-film material and facilitates the interpretation of the evolution of its electrical properties. This knowledge will be key for optimizing future BTO devices and might also lead to a better understanding of ALD ternary MO films in general.

■ ASSOCIATED CONTENT

ⓈSupporting Information

The Supporting Information is available free of charge on the ACS Publications website at DOI: 10.1021/acs.jpclett.6b00393.

> Details on the ALD deposition parameters, experimental measurements, and simulations; Ti K-, Ti L3- and L2-, and Ba M5 and M4-edge as well as grazing incidence X-ray diffraction spectra on annealed BTO thin films (PDF)

■ AUTHOR INFORMATION

Author Contributions

[⊥]J.T., S.A., and A.D. contributed equally to this work.

Notes

The authors declare no competing financial interest.

■ ACKNOWLEDGMENTS

■ REFERENCES

(1) Sreenivas, K.; Mansingh, A.; Sayer, M. Structural and Electrical Properties of Rf-sputtered Amorphous Barium Titanate Thin Films. *J. Appl. Phys.* **1987**, *62*, 4475−4481.

(2) Urban, J. J.; Yun, W. S.; Gu, Q.; Park, H. Synthesis of Single-Crystalline Perovskite Nanorods Composed of Barium Titanate and Strontium Titanate. *J. Am. Chem. Soc.* **2002**, *124*, 1186−1187.

(3) Lee, H. N.; Christen, H. M.; Chisholm, M. F.; Rouleau, C. M.; Lowndes, D. H. Strong Polarization Enhancement in Asymmetric Three-Component Ferroelectric Superlattices. *Nature* **2005**, *433*, 395−399.

(4) Jaffe, B.; Cook, W. R.; Jaffe, H. Chapter 5: Barium Titanate. In *Piezoelectric Ceramics*; Roberts, J. P., Popper, P., Eds.; Academic Press: New York, 1971; pp 53−114.

(5) Feinberg, J.; Heiman, D.; Tanguay, A. R., Jr.; Hellwarth, R. W. Photorefractive Effects and Light-induced Charge Migration in Barium Titanate. *J. Appl. Phys.* **1980**, *51*, 1297−1305.

(6) Acharya, S.; Torgersen, J.; Kim, Y.; Park, J.; Schindler, P.; Dadlani, A. L.; Winterkorn, M. M.; Xu, S.; Walch, S. P.; Usui, T.; et al. Self-Limiting Atomic Layer Deposition of Barium Oxide and Barium Titanate Thin Films Using a Novel Pyrrole Based Precursor. *J. Mater. Chem. C* **2016**, *4*, 1945−1952.

(7) Schindler, P.; Kim, Y.; Thian, D.; An, J.; Prinz, F. B. Plasma-Enhanced Atomic Layer Deposition of $BaTiO_3$. *Scr. Mater.* **2016**, *111*, 106−109.

(8) Vehkamäki, M.; Hatanpää, T.; Ritala, M.; Leskelä, M.; Väyrynen, S.; Rauhala, E. Atomic Layer Deposition of $BaTiO_3$ Thin Films— Effect of Barium Hydroxide Formation. *Chem. Vap. Deposition* **2007**, *13*, 239−246.

(9) Johnson, R. W.; Hultqvist, A.; Bent, S. F. A Brief Review of Atomic Layer Deposition: From Fundamentals to Applications. *Mater. Today* **2014**, *17*, 236−246.

(10) George, S. M. Atomic Layer Deposition: An Overview. *Chem. Rev.* **2010**, *110*, 111−131.

(11) Schindler, P.; Logar, M.; Provine, J.; Prinz, F. B. Enhanced Step Coverage of TiO_2 Deposited on High Aspect Ratio Surfaces by Plasma-Enhanced Atomic Layer Deposition. *Langmuir* **2015**, *31*, 5057−5062.

(12) Lee, S. W.; Han, J. H.; Han, S.; Lee, W.; Jang, J. H.; Seo, M.; Kim, S. K.; Dussarrat, C.; Gatineau, J.; Min, Y.-S.; et al. Atomic Layer Deposition of $SrTiO_3$ Thin Films with Highly Enhanced Growth Rate for Ultrahigh Density Capacitors. *Chem. Mater.* **2011**, *23*, 2227−2236.

(13) Elam, J. W.; Sechrist, Z. A.; George, S. M. ZnO/Al_2O_3 Nanolaminates Fabricated by Atomic Layer Deposition: Growth and Surface Roughness Measurements. *Thin Solid Films* **2002**, *414*, 43−55.

(14) Lee, D.-J.; Kim, H.-M.; Kwon, J.-Y.; Choi, H.; Kim, S.-H.; Kim, K.-B. Structural and Electrical Properties of Atomic Layer Deposited Al-Doped ZnO Films. *Adv. Funct. Mater.* **2011**, *21*, 448−455.

(15) Thimsen, E.; Baryshev, S. V.; Martinson, A. B. F.; Elam, J. W.; Veryovkin, I. V.; Pellin, M. J. Interfaces and Composition Profiles in Metal−Sulfide Nanolayers Synthesized by Atomic Layer Deposition. *Chem. Mater.* **2013**, *25*, 313−319.

(16) Miikkulainen, V.; Leskela, M.; Ritala, M.; Puurunen, R. L. Crystallinity of Inorganic Films Grown by Atomic Layer Deposition: Overview and General Trends. *J. Appl. Phys.* **2013**, *113*, 021301.

(17) An, J.; Usui, T.; Logar, M.; Park, J.; Thian, D.; Kim, S.; Kim, K.; Prinz, F. B. Plasma Processing for Crystallization and Densification of Atomic Layer Deposition $BaTiO_3$ Thin Films. *ACS Appl. Mater. Interfaces* **2014**, *6*, 10656−10660.

(18) Kim, H.; McIntyre, P. C.; Saraswat, K. C. Effects of Crystallization on the Electrical Properties of Ultrathin HfO_2 Dielectrics Grown by Atomic Layer Deposition. *Appl. Phys. Lett.* **2003**, *82*, 106.

(19) Li, P.; Lu, T.-M.; Bakhru, H. High Charge Storage in Amorphous $BaTiO_3$ Thin Films. *Appl. Phys. Lett.* **1991**, *58*, 2639−2641.

(20) Chattopadhyay, S.; Teren, A. R.; Hwang, J.-H.; Mason, T. O.; Wessels, B. W. Diffuse Phase Transition in Epitaxial $BaTiO_3$ Thin Films. *J. Mater. Res.* **2002**, *17*, 669−674.

(21) Kim, Y. S.; Jo, J. Y.; Kim, D. J.; Chang, Y. J.; Lee, J. H.; Noh, T. W.; Song, T. K.; Yoon, J.-G.; Chung, J.-S.; Baik, S. I.; et al. Ferroelectric Properties of $SrRuO_3/BaTiO_3/SrRuO_3$ Ultrathin Film Capacitors Free from Passive Layers. *Appl. Phys. Lett.* **2006**, *88*, 072909.

(22) Dadlani, A. L.; Trejo, O.; Acharya, S.; Torgersen, J.; Petousis, I.; Nordlund, D.; Sarangi, R.; Schindler, P.; Prinz, F. B. Exploring Local

Electronic Structure and Geometric Arrangement of ALD Zn(O,S) Buffer Layers Using X-Ray Absorption Spectroscopy. *J. Mater. Chem. C* **2015**, *3*, 12192−12198.

(23) Trejo, O.; Roelofs, K. E.; Xu, S.; Logar, M.; Sarangi, R.; Nordlund, D.; Dadlani, A. L.; Kravec, R.; Dasgupta, N. P.; Bent, S. F.; et al. Quantifying Geometric Strain at the PbS QD-TiO$_2$ Anode Interface and Its Effect on Electronic Structures. *Nano Lett.* **2015**, *15*, 7829−7836.

(24) Balerna, A.; Bernieri, E.; Burattini, E.; Kuzmin, A.; Lusis, A.; Purans, J.; Cikmach, P. EXAFS Studies of MeO$_{3−x}$ (Me = W, Mo, Re, Ir) Crystalline and Amorphous Oxides. *Nucl. Instrum. Methods Phys. Res., Sect. A* **1991**, *308*, 234−239.

(25) Boichot, R.; Tian, L.; Richard, M.-I.; Crisci, A.; Chaker, A.; Cantelli, V.; Coindeau, S.; Lay, S.; Ouled, T.; Guichet, C.; et al. Evolution of Crystal Structure During the Initial Stages of ZnO Atomic Layer Deposition. *Chem. Mater.* **2016**, *28*, 592−600.

(26) Billinge, S. J. L.; Levin, I. The Problem with Determining Atomic Structure at the Nanoscale. *Science* **2007**, *316*, 561−565.

(27) Rehr, J. J.; Kas, J. J.; Prange, M. P.; Sorini, A. P.; Takimoto, Y.; Vila, F. Ab Initio Theory and Calculations of X-Ray Spectra. *C. R. Phys.* **2009**, *10*, 548−559.

(28) Rehr, J. J.; Kas, J. J.; Vila, F. D.; Prange, M. P.; Jorissen, K. Parameter-Free Calculations of X-Ray Spectra with FEFF9. *Phys. Chem. Chem. Phys.* **2010**, *12*, 5503−5513.

(29) Bugnet, M.; Radtke, G.; Botton, G. A. Oxygen 1 S Excitation and Tetragonal Distortion from Core-Hole Effect in BaTiO$_3$. *Phys. Rev. B: Condens. Matter Mater. Phys.* **2013**, *88*, 201107.

(30) Wu, Z.; Langenhorst, F.; Seifert, F.; Paris, E.; Marcelli, A. Oxygen 1s ELNES Study of Perovskites (Ca, Sr, Ba) TiO3. *J. Synchrotron Radiat.* **2001**, *8*, 934−936.

(31) Chassé, A.; Borek, St.; Schindler, K.-M.; Trautmann, M.; Huth, M.; Steudel, F.; Makhova, L.; Gräfe, J.; Denecke, R. High-Resolution X-Ray Absorption Spectroscopy of BaTiO 3: Experiment and First-Principles Calculations. *Phys. Rev. B: Condens. Matter Mater. Phys.* **2011**, *84*, 195135.

(32) Choi, K. J.; Biegalski, M.; Li, Y. L.; Sharan, A.; Schubert, J.; Uecker, R.; Reiche, P.; Chen, Y. B.; Pan, X. Q.; Gopalan, V.; et al. Enhancement of Ferroelectricity in Strained BaTiO$_3$ Thin Films. *Science* **2004**, *306*, 1005−1009.

(33) Gougousi, T.; Ye, L. Interface Between Atomic Layer Deposition Ta$_2$O$_5$ Films and GaAs(100) Surfaces. *J. Phys. Chem. C* **2012**, *116*, 8924−8931.

(34) Tsai, H. M.; Babu, P. D.; Pao, C. W.; Chiou, J. W.; Jan, J. C.; Krishna Kumar, K. P.; Chien, F. Z.; Pong, W. F.; Tsai, M.-H.; Chen, C.-H.; et al. Comparison of Electronic Structures of RuO$_2$ and IrO$_2$ Nanorods Investigated by X-Ray Absorption and Scanning Photoelectron Microscopy. *Appl. Phys. Lett.* **2007**, *90*, 042108.

(35) Zhou, J. G.; Fang, H. T.; Hu, Y. F.; Sham, T. K.; Wu, C. X.; Liu, M.; Li, F. Immobilization of RuO$_2$ on Carbon Nanotube: An X-Ray Absorption near-Edge Structure Study. *J. Phys. Chem. C* **2009**, *113*, 10747−10750.

(36) Tamura, T.; Tanaka, S.; Kohyama, M. Full-PAW Calculations of XANES/ELNES Spectra of Ti-Bearing Oxide Crystals and TiO-SiO Glasses: Relation between Pre-Edge Peaks and Ti Coordination. *Phys. Rev. B: Condens. Matter Mater. Phys.* **2012**, *85*, 205210.

(37) Han, J. H.; Lee, W.; Jeon, W.; Lee, S. W.; Hwang, C. S.; Ko, C.; Gatineau, J. Growth of Conductive SrRuO$_3$ Films by Combining Atomic Layer Deposited SrO and Chemical Vapor Deposited RuO 2 Layers. *Chem. Mater.* **2012**, *24*, 4686−4692.

(38) Nix, W. D. Mechanical Properties of Thin Films. *Metall. Trans. A* **1989**, *20*, 2217−2245.

(39) Blanchard, P. E. R.; Liu, S.; Kennedy, B. J.; Ling, C. D.; Zhang, Z.; Avdeev, M.; Jang, L.-Y.; Lee, J.-F.; Pao, C.-W.; Chen, J.-L. Studying the Effects of Zr-Doping in (Bi$_{0.5}$Na$_{0.5}$)TiO$_3$ via Diffraction and Spectroscopy. *Dalton Trans.* **2014**, *43*, 17358−17365.

(40) Jang, J. W.; Chung, S. J.; Cho, W. J.; Hahn, T. S.; Choi, S. S. Thickness Dependence of Room Temperature Permittivity of Polycrystalline BaTiO$_3$ Thin Films by Radio-Frequency Magnetron Sputtering. *J. Appl. Phys.* **1997**, *81*, 6322.

(41) Liu, M.; Ma, C.; Collins, G.; Liu, J.; Chen, C.; Dai, C.; Lin, Y.; Shui, L.; Xiang, F.; Wang, H.; et al. Interface Engineered BaTiO$_3$/SrTiO$_3$ Heterostructures with Optimized High-Frequency Dielectric Properties. *ACS Appl. Mater. Interfaces* **2012**, *4*, 5761−5765.

(42) Kim, J.; Krishnan, S. A.; Narayanan, S.; Chudzik, M. P.; Fischetti, M. V. Thickness and Temperature Dependence of the Leakage Current in Hafnium-Based Si SOI MOSFETs. *Microelectron. Reliab.* **2012**, *52*, 2907−2913.

(43) Tapily, K.; Jakes, J.; Shrestha, P. R.; Gu, D.; Baumgart, H.; Elmustafa, A. Comparison of Nanomechanical Behavior of the Amorphous and Crystalline Phases of ALD HfO$_2$. *ECS Trans.* **2008**, *16*, 269−277.

(44) Eng, H. W.; Barnes, P. W.; Auer, B. M.; Woodward, P. M. Investigations of the Electronic Structure of d0 Transition Metal Oxides Belonging to the Perovskite Family. *J. Solid State Chem.* **2003**, *175*, 94−109.